Reactive and Functional Polymers 194 (2024) 105778

Contents lists available at ScienceDirect

Reactive and Functional Polymers

journal homepage: www.elsevier.com/locate/react

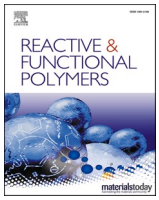

In silico and experimental study of functionalized monomer for molecularly imprinted-enoxaparin polymer: A novel green approach

Engrid Juni Astuti [a,e], Benny Permana [a], Slamet Ibrahim [b], Muhammad Ali Zulfikar [c], Sophi Damayanti [a,d,*]

[a] *Department of Pharmacochemistry, School of Pharmacy, Institut Teknologi Bandung, Bandung 40132, Indonesia*
[b] *Faculty of Pharmacy, Universitas Jenderal Achmad Yani, Cimahi 40633, Indonesia*
[c] *Division on Analytical Chemistry, Faculty of Mathematics and Natural Sciences, Institut Teknologi Bandung, Bandung 40132, Indonesia*
[d] *University Center of Excellence on Artificial Intelligence for Vision, Natural Language Processing & Big Data Analysis (U-CoE AI-VLB), Institut Teknologi Bandung, Bandung 40132, Indonesia*
[e] *Department of Pharmacy, Faculty of Health Sciences, Universitas Muhammadiyah Malang, Malang 65145, Indonesia*

ARTICLE INFO

Keywords:
Enoxaparin
In silico study
MIP
Green chemistry
Microwave synthesizer workstation

ABSTRACT

Enoxaparin (enox) is a low molecular weight heparin. Enox, which has side effects of thrombocytopenia and bleeding, requires monitoring drug therapy. The analysis method of enox in the blood plasma matrix needs a prior separation method. There has not been a molecularly imprinted polymer (MIP) synthesis for enox in earlier studies. Therefore, a novel MIP of enox was synthesized *via* microwave synthesizer workstation. This research aims to examine the application of *in silico* studies in selecting functional monomers and their comparison with enoxaparin before carrying out MIP synthesis. Enox as a template was polymerized with itaconic acid (ITA) as the best functional monomer; *N*,*N*′-methylenebisacrylamide as a cross-linking agent; water as a porogen; and ammonium persulfate as an initiator. Itaconic acid was selected using the *in silico* to calculate binding energy, and Gibbs free energy gives the smallest values. Itaconic acid and enoxaparin ratio was computed using DFT, and GFN2-xTB found that 1:6 was the best ratio. For calculations using molecular dynamics simulations, it was found that a ratio of 1:1 was the best, the same as in laboratory experiments using the job's plot. Polymerization was performed using a microwave at room temperature (28 °C) with an ITA ratio of 1:1, 1:4, and 1:6. Nonimprinted polymers (NIP) were similarly prepared without a template as a control. All polymer particles were characterized by spectral (Fourier-transform infrared spectroscopy), thermal (thermogravimetric analysis–differential thermal gravimetry), and morphology (scanning electron microscope). The adsorption capacity for enox was carried out with MIP and NIP. The performance of MIP was evaluated by determining the imprinting factors calculated. The MIP 1:1, 1:4, and 1:6 displayed imprinting factor is 1.21, 0.68, and 0.68, respectively. The best ratio of ITA to Enox is 1:1.

1. Introduction

Enoxaparin (enox), a low molecular weight heparin, has a higher bioavailability and a longer half-life than unfractionated heparin (UFH). Compare to UFH, enox are its easier to apply and a lower tendency of bleeding problems. Enox can exert anti-inflammatory effects and partially attenuate the cytokine storm caused by the virus in patients with COVID-19, especially in patients with severe symptoms [1–4]. Enox, which has side effects of thrombocytopenia and bleeding, requires monitoring drug therapy. This process requires an analysis method of enox in the blood plasma matrix. Some of the testing methods for enox involve using high-performance liquid chromatography with a size exclusion column, a fluorescence sensor, spectrofluorometry for anti-Xa testing, and sensors [5–7].

Applying sample preparation in biological matrices often involves lengthy procedures and yields low recovery rates. Molecularly imprinted polymers (MIP) are introduced as synthetic receptors that mimic the specificity and selectivity of biological receptors. MIP has the same properties as antigen and antibodies, where MIP is the antibody and the template compound is the antigen offering advantages such as enhanced resistance to environmental, chemical and degradation condition, speed and ease of synthesis, selective adsorption, high sensitivity, high

* Corresponding author at: Department of Pharmacochemistry, School of Pharmacy, Institut Teknologi Bandung, Bandung 40132, Indonesia.
E-mail address: sophi.damayanti@itb.ac.id (S. Damayanti).

https://doi.org/10.1016/j.reactfunctpolym.2023.105778
Received 30 June 2023; Received in revised form 1 November 2023; Accepted 9 November 2023
Available online 13 November 2023

structural stability, ability to be store for years without loss of efficiency and wide range of application in detecting different analytes and lower cost, [8–14]. MIP involves mass transfer adsorption, with the adsorbate moving to the adsorbent's surface. Adsorption was regulated by the adsorbent, operational conditions, adsorbate, and thermodynamic parameters [15]. Green chemistry advocates for the reduction of toxic reagents and solvents, energy conservation, and operator safety. Water emerges as a favorable solvent in chemical reactions due to its numerous benefits, including improved reactivity, simplified workup processes, catalyst recyclability, mild reaction conditions without protective groups, and inherent environmental friendliness. However, synthesizing MIPs for macromolecules such as enox presents challenges because they dissolve in water, limiting the selection of functional monomers (FMs) and cross-linkers. Water as a solvent disrupts hydrogen bonds (H-bonds) between monomers and the template, making template removal more difficult. Additionally, biological macromolecules adhere to the hydrophobic surface of MIPs *via* hydrophobic interactions, leading to decreased selectivity [16–19].

Manufacturing MIP involves several stages: assembly, polymerization, removal of the analyte or template, and binding of the analyte or template. Polymerization of MIP typically involves traditional heating, photopolymerization, ultrasonic, and microwave methods. The use of microwaves for polymerization has several advantages, including uniform heating, rapid speed, energy efficiency, and high efficiency, as microwave energy can transfer electromagnetic waves into the material [20]. MIP synthesis requires microwave radiation to increase reaction speeds, product yield, and clean processes. Microwave synthesizer workstations end faster than chemical reactions, which take hours or days [21,22]. In this paper, we synthesized a novel MIP for enox using microwave synthesizer workstation. We used water as a solvent and chose an FM using *in silico* study.

2. Materials and methods

2.1. Materials

The materials used in this study were enox sodium (BetaPharma Co. Ltd., Shanghai, China), itaconic acid (ITA), and ammonium persulfate ($NH_4S_2O_8$) (Sigma-Aldrich, St. Louis, MO, USA), *N*,*N*′-methylenebisacrylamide (MBAA) (Tokyo Chemical Industry, Tokyo, Japan), and water for injection (IKA Pharma, Indonesia). Synthesis of MIP and nonimprinted polymer (NIP) by microwave synthesizer workstation (Sineo MAS-II, Shanghai, China). Moreover, the characterization of the material was performed using Fourier-transform infrared (FTIR) spectroscopy (Jasco-4200 type A, Japan), a KBr plate, a KBr pellet press tool (Jasco Minipress MP-1), an oven KBr (Memmert), a scanning electron microscope (SEM; Hitachi SU 3500, Hitachi, Tokyo, Japan), thermal (thermogravimetric analysis [TGA]–differential thermal gravimetry [DTG]) (Hitachi STA7300 Hitachi, Tokyo, Japan), and spectrophotometer UV–Vis (Agilent, Santa Clara, CA, USA). Gaussian 09 W version 8.0 and Gauss view 5.0 were used in this study (Gaussian Inc., Wallingford, CT, USA; license owned by the School of Pharmacy, Institut Teknologi Bandung). GFN2-xTB free software (Bonn University, Germany) and YASARA version 22.9.24.W.64 (YASARA Biosciences GmbH, Austria; license owned by engridjuni81@umm.ac.id).

2.2. In silico experiments

2.2.1. Optimization geometry

The structure (Fig. 1) used in this study were two-dimensional structures of enox as a template, and ITA, methacrylic acid, methacrylamide, acrylamide, acrylic acid, allylamine (allyl), 2-aminoethyl methacrylate, n-isopropyl acrylamide, 1-vinyl imidazole, and 2-(trifluoromethyl)acrylic acid as FMs. The FM used in this study is a water-soluble FM because enox can only be dissolved in water. The structure was obtained from www.pubchem.ncbi.nlm.nih.gov in .sdf format. After that, the structure changed to be three-dimensional using Avogadro and saved in PDB format for input Gaussian® and .xyz format for input GFN2-xTB. The optimization of structures, energy minimization, transformation, and frequency in PDB structure format using Gaussian®. Calculate *ab initio* using restricted Hartree–Fock (RHF) theory with basis set 3-21G and DFT using B3LYP theory with basis set 3-21G. The optimization of structures, minimization energy, transformation, and frequency using GFN2-xTB software.

The process of molecular docking between enox and FM was conducted using MGLTools® 1.5.6, which is coupled with AutoDock® 4.2 software. The complex of enox with FM was chosen by good energy interaction. After that, the results were visualized using BIOVIA Discovery Studio® 2020 and saved in PDB and .xyz formats for Gaussian and GFN2-xTB software, respectively. The best molecular docking conformation of the complex continued to optimization structure using Gaussian for *ab initio* and DFT and obtain the energy binding (E) and

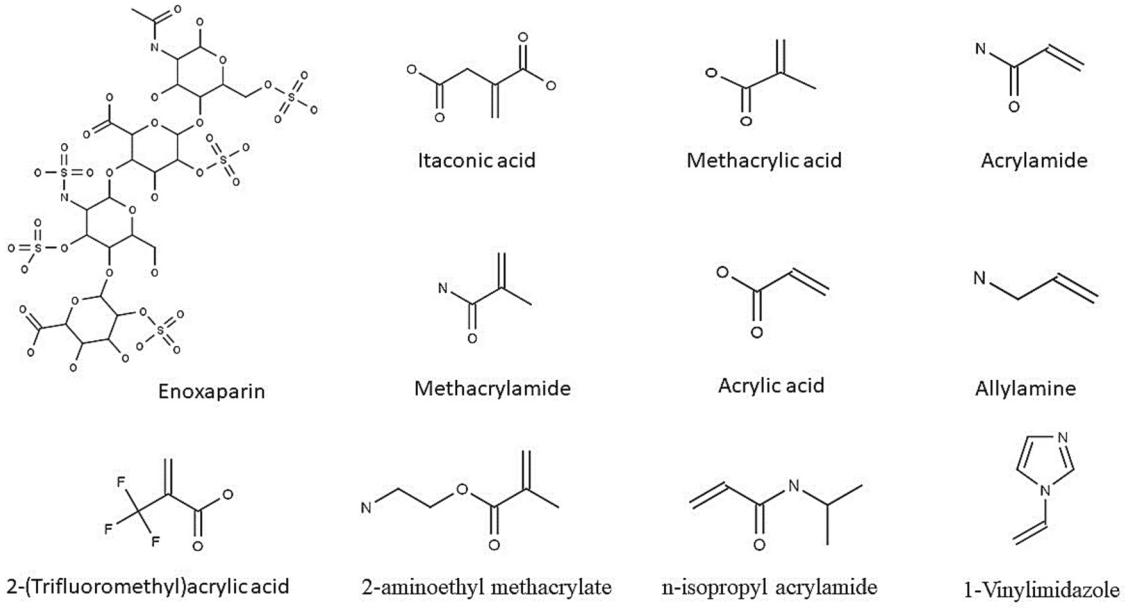

Fig. 1. Structure of enox and FM.

energy Gibs (G) for the complex structure from 1:1. The best ratio interaction enox with FM can calculate E complex from 1:1 until 1:10 using DFT and E and G complex using GFN2-xTB. After that, calculate ΔE and ΔG using eqs. (1) and (2), respectively.

$$\Delta E = E_{complex} - (E_{enox} + n.E_{FM}) \quad (1)$$

$$\Delta G = G_{complex} - (G_{enox} + n.G_{FM}) \quad (2)$$

2.2.2. Molecular dynamics

The best ratio interaction enox with FM calculate with molecular dynamic (MD) simulation from 1:1 until 1:10 using YASARA®. Enox and ITA conformed best in a cubic box of water molecules at 301 °K and 0.997 g/mL. The MD calculated root-mean-square deviation (RMSD), radius of gyration (Rg), and H-bond.

2.2.3. Job's plot

The experiment binding used a Job's plot for enox with the best FM from *in silico* study. First, we chose the best solvent for enox to obtain spectra at spectrophotometry UV–Vis. Enox and FM diluted in water with the same rasio/molaritas. After that, make a combined volume with a total volume of 4 mL. Read the absorbance of all combination volumes using spectrophotometric UV–Vis. Calculate the ratio using a polynomial to obtain the best ratio of enox and FM. The calculation also used the intersection of two regression lines.

2.3. Synthesis

2.3.1. Optimization synthesis of MIP and NIP

MIP was synthesized using a microwave synthesizer workstation. In a bottle, 0.1, 0.4, or 0.6 mmol ITA and 2 mmol MBAA were dissolved in 25 mL of water and sonicated for 25 min. To the mixture, 0.1 mmol of enox and 1% of $NH_4S_2O_8$ were added and shaken. The mixture is transferred to a three-neck flask, placed in the microwave synthesizer workstation, and ran on nitrogen gas. Microwave synthesizer workstasion for time, power magnetic resonance, and stirring were set to 90 min, 300 watts, and 400 rpm, respectively. NIP was produced identically, excluding the addition of the template enox. To remove the template, 100 mg MIP was sonicated with 10 mL water. The technique was continued until the UV–Vis spectrum showed no enox peaks. After synthesis, the polymer was dried at 40 °C. The synthesis procedure is illustrated in Fig. 2.

2.3.2. Characterizations

The thermal stability of enox and the polymer particles from NIP and MIP were assessed using TGA and DTG to characterize MIP and NIP. The temperature ranged from 24 °C to 300 °C. The surface structure of MIP and NIP was analyzed using SEM. Prior to SEM analysis, the sample was affixed to a metal plate that had been covered with a layer of gold in a vacuum. The scanning process was performed using a current of 60 mA and an electric potential of 15 Volts. The produced polymer was further analyzed using FTIR spectroscopy with a wave number range of 400–4000 cm^{-1}. Subsequently, the FTIR spectrums of the MIP and NIP were paired with the spectra of the individual components.

2.3.3. Adsorption capacity

Experimental approach for enox adsorption from aqueous solution. In a 25-mL Erlenmeyer flask, 10 mg of MIP and NIP with ratios 1:1, 1:4, and 1:6 were mixed with 10 mL of 300 ppm enox and agitated at 100 rpm for 180 min. All filtrate was filtered using a 0.45-μm nylon membrane. 6 mL filtrate pipette, transfer to 10 mL volumetric flask and add 1 mL HCl 0.1 N and water until 10 mL. Spectrophotometry UV–Vis measured it at wavelength 231 nm. Eq. (3) was used to determine adsorption capacity. MIP performance was assessed by calculating imprinting factors using eq. (4).

$$qe = \frac{(Ci - Cf)V}{m} \quad (3)$$

$$IF = \frac{qe_m}{qe_n} \quad (4)$$

where qe is the adsorption capacity (mg g^{-1}), V is the volume of the

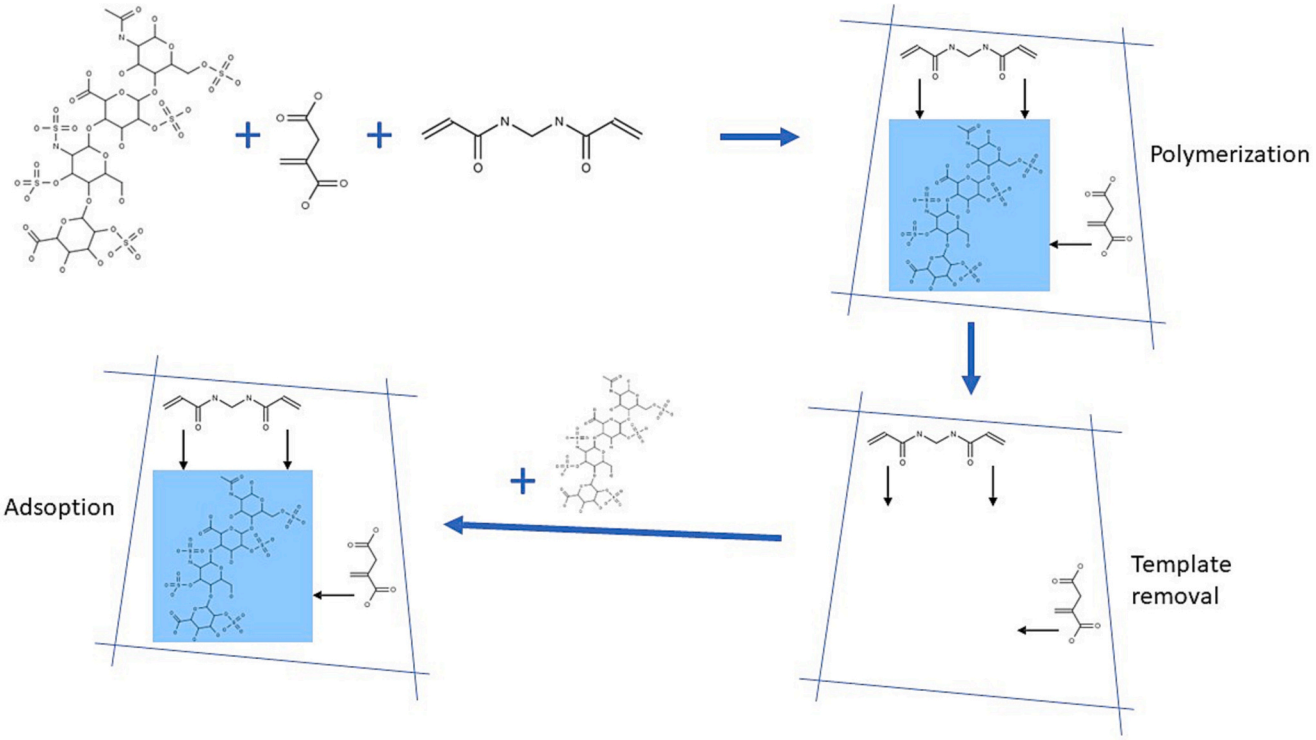

Fig. 2. Schematic procedures of MIP synthesis.

solution (L), *Ci* is the initial concentration of enox (mg L^{-1}), *Cf* is the final concentration of enox (mg L^{-1}), *m* is the MIP/NIP mass (g), *IF* is the imprinting factor, qe_m and qe_n are the adsorption capacities of MIP and NIP, respectively.

3. Results and discussion

3.1. In silico studies

3.1.1. Optimization geometry

Selection of the best FM in this experiment used *ab initio* and DFT. The *ab initio* MIP design utilizes HF/6-31G(d) and HF/3-21G. This approach has mostly been used to choose the best FM by estimating the monomer–template complex binding energy with various FM. Highest negative value indicates strongest interaction. Additionally, this method has also been used to get the optimal FM ratio template from binding energies by considering multiple ratios. According to the principle, choosing the FM with the largest ΔE is more likely to generate a strong complex with the template. HF/3-21G was used in this research because it matches simulation and experimental results and has lower processing costs [23].

DFT-based approaches have replaced *ab initio* methods because they are faster and more efficient. For calculating and simulating numerous molecule interactions, DFT methods with hybrid functions and basis sets are most accurate. However, molecular mechanics simulates interactions and calculates binding energies better for systems with atoms or big molecules [24]. Enox, which has a large molecular with 112 atoms, is more difficult to calculate using DFT, so it takes a long time. Modelling using computation for monomer-template formation in a solution can be modelled relatively easily. Still, the challenge lies in modelling different polymerization stages, including cross-linker compounds added in the polymerization stage. Therefore, computational protocol improvements are needed in further research to explain the differences between predicted results and experiments [25]. Electronic energy, Gibbs free energy, enthalpy, and entropy determine thermodynamic feasibility. Calculating frequency at 5–400 °K yields this thermodynamic parameter. Due to the predictability of chemical processes at constant temperature, Gibbs free energy calculations are significant. The basis set superposition error correction in energy is included. Enthalpy and entropy changes encourage reaction spontaneity and free energy. Temperature raises entropy. Molecule atoms with more kinetic energy heat up. Slower-moving atoms and particles have less chaos at lower temperatures. The sign of ΔG must be negative since spontaneous reactions release free energy. Results indicate a negative ΔG, indicating favorable conditions for the reaction process [26]. For this study, we used *ab initio* using RHF with basis set 3-21G and DFT B3LYP with basis set 3-21G. The results of ΔE and ΔG are shown in Table 1. The calculation of ΔE and ΔG using *ab initio* and DFT can be seen as the best FM is ITA. Three H-bonds formed between enox and ITA using *ab initio* and DFT. Noncovalent imprinting is the most commonly used imprint to stabilize the template–monomer complex *via* hydrogen bonding, making it flexible when the template is removed [27,28]. We can predict the type of interaction between enox and ITA based on the structure. The interaction between ITA and enox can be noncovalent due to the presence of oxygen, which can act as a hydrogen acceptor, forming a hydrogen bond between the carboxyl group and the hydroxyl of the carboxylic acid group that both have. The formed H-bonds are shown in Fig. 3.

Table 1
ΔE and ΔG with ratio 1:1 enox between FM using *ab initio* and DFT.

No	Functional monomer	*Ab initio*		DFT	
		ΔE	ΔG	ΔE	ΔG
1	Acrylamide	−43.6791	−25.3351	−30.3872	−14.0336
2	Acrylic acid	−25.5328	−12.1423	−33.6151	−16.1101
3	2-Aminoethyl methacrylate	−23.6283	−5.9419	−9.3988	4.1183
4	Allylamine	−37.4065	−23.1106	−35.0044	−16.2393
5	n-isopropyl acrylamide	−38.4212	−24.1416	−21.0097	−3.7726
6	Itaconic acid	**−45.6419**	**−30.1186**	**−62.3199**	**−40.8691**
7	2-(Trifluoromethyl) acrylic acid	−33.2907	−17.7290	−29.2658	−11.3021
8	1-Vinyl imidazole	−38.1200	−22.3538	−25.0144	−9.7289
9	Methacrylamide	−41.9472	−26.5857	−46.3529	−29.1573
10	Methacrylic acid	−43.1043	−29.0895	−27.2948	−11.7577

The next step was a calculation of the molar ratio enox between ITA using DFT and GFN2-xTB. Calculation molar ratio enox with ITA was calculated ΔE using Gaussian DFT with the same method when calculating the best FM. GFN2-xTB is a semiempirical quantum mechanical approach for rapidly calculating the structure and energy of noncovalent interactions for molecular systems with approximately 1000 atoms. The effect of anisotropic second-order fluctuations from short-range interactions of generated atomic multipole moments makes GFN2-xTB unique. The accuracy of this method is used as a benchmark for various systems and compared with that of other semiempirical methods. Its high computational efficiency and improved physics compared with those of its predecessor GFN-xTB make this method particularly suitable for exploring the conformational space of molecular systems. Grimme and coworkers developed the semiempirical GFN2-xTB method. A comparison of GFN2-XTB with other methodologies also attests to the extended tight binding approach's strong appeal and low computational cost [29,30].

In this research, GFN2-xTB was used to calculate the frequency to obtain the Gibbs free energy, whereas in calculations using DFT, the Gibbs free energy could not be calculated because the enox was too large molecule with the addition of more and more ITA. The analysis of ΔE and ΔG using GFN2-xTB was expected to provide the best ratio calculation results for ITA and enox, the same as calculating ΔE using DFT. Calculations added water as a solvent to be used in MIP when calculating GFN2-xTB. The water phase is also calculated on the basis of the temperature at 301 K to assess the stability of the reaction when temperatures are used. The temperature was chosen because enox is not stable to heat. Gibbs free energy is a distinctive function that minimizes under constant temperature and pressure, which are frequently regulated during experiments [31]. The results of ΔE ratio enox between ITA using DFT and ΔE and ΔG ratio enox between ITA using GFN2-xTB are shown in Table 2. The best ratio is 1:6 using DFT and GFN2-xTB. ΔG with a range minus 15–30 kcal/mol has a strong H-bond. On the basis of ΔG, it can be seen that at a temperature of 301 K, the reaction can run more spontaneously than at room temperature because enox is stable below room temperature.

3.1.2. Calculation of molar ratio enox between ITA using MD

Calculation molar ratio enox with ITA was calculated RMSD, Rg, and H-bond using MD simulation. An MD simulation utilizing YASARA (22.9.24.W.64) software determined the best conformational stability for enox and ITA. Enox and ITA with a ratio of 1:1 to 1:10 were placed in the center of a virtual box with defined dimensions, which was then filled with water until its maximum capacity. The simulation was run at a standard pace (2 × 1.25 fs time step). After the steepest descent and simulated annealing minimizations, AMBER14 Force Field simulations lasted 200 ns [32–34]. This experiment used water as a porogen in the MD simulation to observe a significant affinity for the interaction between enox and ITA. Strong template and FM bonding are required to imprint a polymeric matrix successfully. However, the bonding is insufficient because the porogen impact must be balanced. To prevent the complex from being displaced by porogen interference or competitive binding, the template's affinity for the porogen should be much weaker than the template's affinity for the monomer [35].

Monitoring the system's equilibrium process and enox structure's stability following the binding of ITA can be achieved by analyzing the

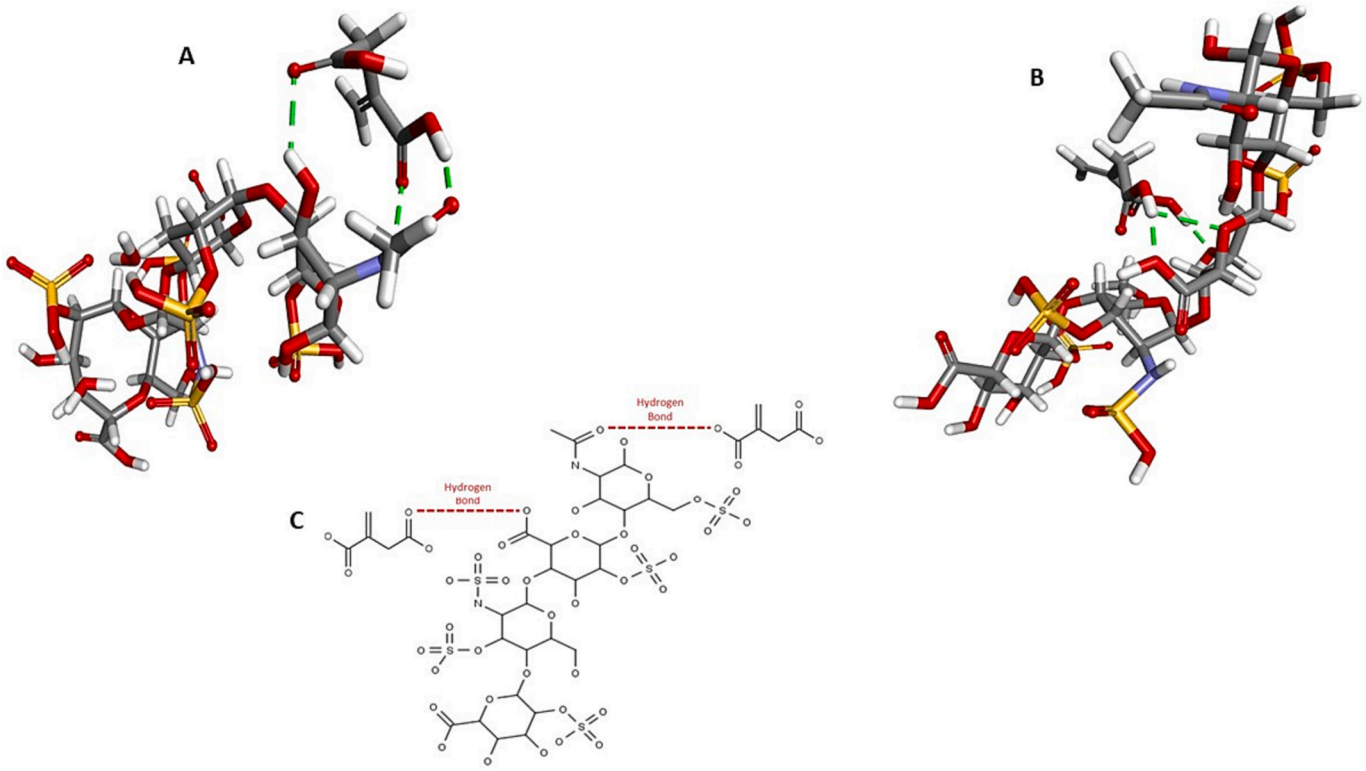

Fig. 3. The hydrogen bond formed between enox and ITA. (A) *Ab initio*, (B) DFT, (C) noncovalent interaction between enox - ITA.

Table 2
ΔE using DFT, ΔE and ΔG using GFN2-xTB of molar ratio enox between ITA.

Ratio complex	DFT	GFN2-xTB	
	ΔE (kcal/mol)	ΔE (kcal/mol)	ΔG (kcal/mol)
Enox	−3,681,887	−250.1485	−156,551
ITA	−308,926	−30.0457	−18,810.2
1:1	−62.3199	−16.6848	1.0906
1:2	−116.0097	22.8987	61.1412
1:3	−117.1586	−18.2774	36.4444
1:4	−150.2767	−73.1102	3.2495
1:5	−180.6884	−34.4846	51.0693
1:6	**−207.0319**	**−122.8963**	**−15.2194**
1:7	−169.6404	−20.9422	94.9274
1:8	−260.4348	−58.7551	76.5173
1:9	−312.3927	−58.5890	92.0871
1:10	−325.6777	−102.2422	67.7357

RMSD over time. In MD simulations, the RMSD is a key measure used to evaluate the structural deviation from the initial enox and ITA structures. Fig. 4 shows that during the 0- to 200-ns period, an upward trend in average RMSD values was observed for ratios ranging from 1:1 to 1:10, with subsequent fluctuations within 6.6 Å for the best ratio 1:1. The calculated average RMSD values indicated that an increased amount of ITA resulted in a significantly higher instability, indicating that the enox exhibited greater flexibility [36,37]. The average RMSD, Rg, and H-bond are shown in Table 3. The Rg analysis was utilized to demonstrate the stability, compactness, folding, and unfolding of the structure being examined. Additionally, Rg was used to evaluate the structural compactness of enox and ITA during the simulation [38]. Analysis of Fig. 3 revealed a clear upward trend in average Rg values ranging from 8.2 to 14.6 Å for ratios 1:1 to 1:10. This observation is attributable to the optimal binding ratio of ITA with enox being 1:1 because higher quantities of ITA result in a less compact structure. Then, an evaluation of H-bond stability during MD simulations was performed. The number of H-bonds in the complexes is crucial for understanding the interaction between enox and ITA. The average number of H-bonds was recorded as 4 (ratios 1:1 to 1:7 and 1:10) and 3 (ratios 1:8 and 1:9) [39].

3.1.3. Job's plot

Spectrophotometry UV titration experiments were conducted to obtain a ratio of enox to ITA. The first time we look for the solvent to obtain a spectrum using spectrophotometry UV. Water and HCl 0,01 N is solvent to look for a spectrum of the enox. HCl 0,01 N is the best solvent for enox, with a maximum wavelength of 231 nm. After that, make a solution of enox and ITA with 0.000228 M concentration, and calculate Job's plot using 10 ratios of volume enox between ITA.

All results are shown in Fig. 5. In the experimental study using titration, the corresponding graph shows a maximum at 0.55 equivalent, indicating the formation complex ratio is 1:1 of enox between ITA using polynomial calculation or the intersection of two regression lines. The use of stoichiometric ratios of template and monomer is not justified because the two species have a strong relationship that needs a lot of solution phase complexes. These complexes finally polymerize, which creates imprinted binding sites. In addition, these polymers must lower nonspecific binding compared to printed polymers made with the fourfold or higher excess that is typical of FMs. This is because there is less chance of randomly distributed functionality beyond the imprinted binding [40].

3.2. Synthesis of MIP and NIP

3.2.1. Optimization synthesis

The synthesis of NIP using ratio enox and ITA (1:4) for optimization of time and power magnetic resonance. This synthesis maintains room temperature (28 °C) due to the stability of enoxaparin as a template. Temperature optimization is not carried out. The ratio was used for the first optimization because it is commonly used for the synthesis of MIP in other experiments. The result optimization in time of microwave is shown in Table 4. For this synthesis, we used the best yield at 90 min.

The second optimization is power magnetic resonance for

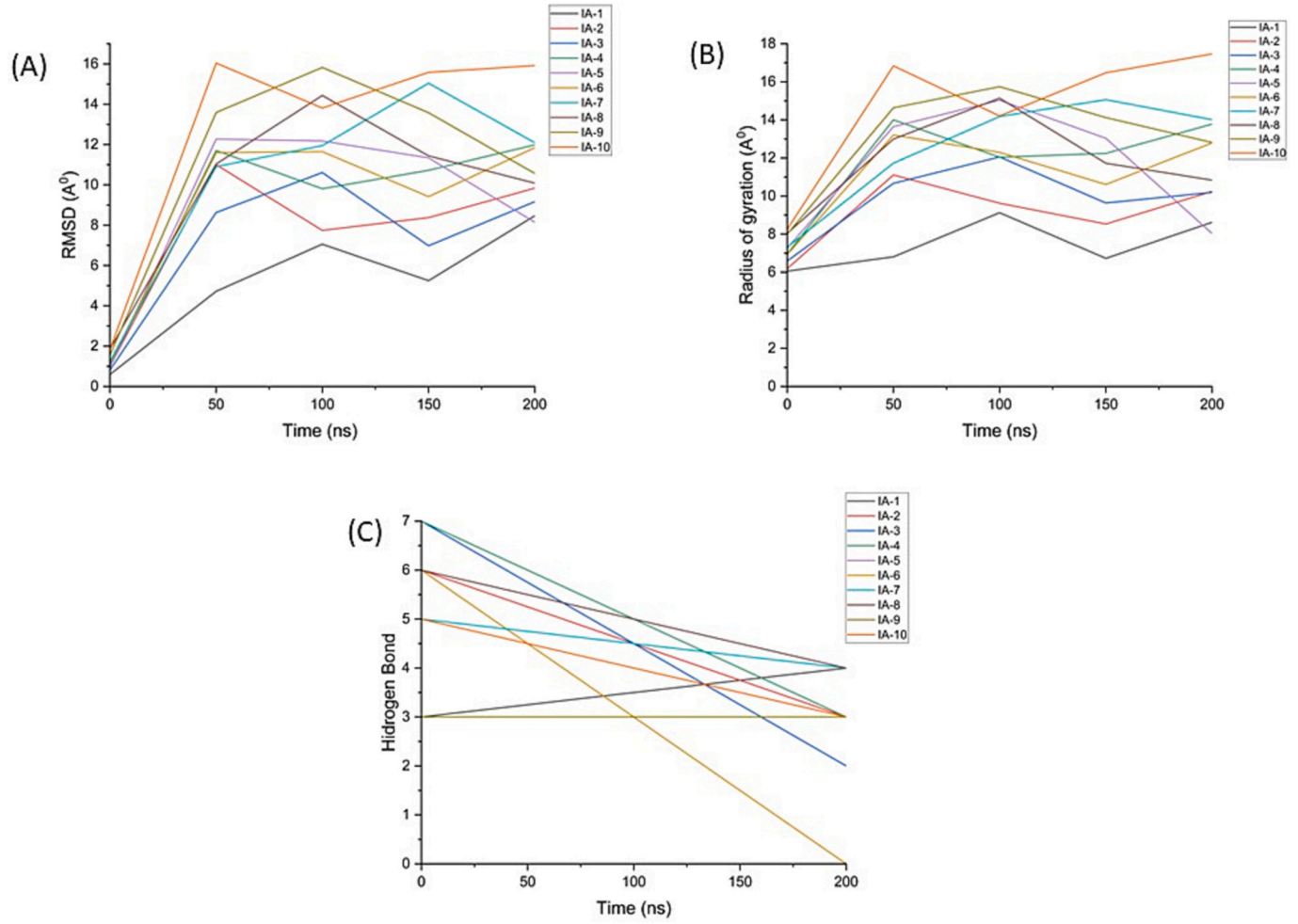

Fig. 4. Result calculation of (A) RMSD, (B) radius of gyration, and (C) HB interaction enox with ITA from ratio 1:1 to 1:10 used MD.

Table 3
RMSD, radius of gyration, and hydrogen bond of molar ratio enox between ITA.

Ratio ITA	Avg RMSD	Avg RG	Avg HB
1	**6.6**	**8.2**	**4**
2	8.4	9.8	4
3	10.0	11.2	4
4	11.6	12.8	4
5	11.4	12.4	4
6	11.8	12.8	4
7	12.9	13.8	4
8	12.3	13.4	3
9	14.0	15.0	3
10	14.0	14.6	4

microwaves. From Table 5, it can be seen that 300 watts is the best power magnetic resonance that can be used for this synthesis. 300 watts is the lowest power that can be set on the microwave device used. The use of greater power is required because the temperature is maintained at room temperature, so it is hoped that this additional power can speed up the time required for synthesis. This is different from the research by Heli A. Brahmbhatt et all [41]; because there is an increase in temperature during synthesis, the magnetic resonance power used is smaller. Apart from that, the solvent used in this research was water, not an organic solvent.

The last optimization is ratio enox with ITA using ratio 1:1 from Job's plot and *in silico* MD, 1:4 from general ratio and 1:6 from *in silico* DFT and GFN2-xTB. The microwave setting was temperature, power magnetic resonance, and time of 28 °C, 300 watts, and 90 min, respectively. As shown in Table 6, the best yield is a ratio of 1:1 for NIP and MIP.

The precipitation polymerization method was used in this study to synthesize MIP and NIP. This method offers advantages over the bulk polymerization method, including the production of spherical and uniform-sized particles, which is particularly beneficial if the sorbent is utilized in chromatography or SPE as it leads to a good separation profile. Additionally, this method eliminates the need for grinding and filtering, which can destroy particles in bulk polymerization [42–44]. All components are soluble in the homogeneous system, which becomes heterogeneous in the continuous phase. Polymer precipitates upon initiation due to insolubleness [45–48].

3.2.2. *Characterization*

3.2.2.1. TGA and DTG. The analysis of TGA can provide unique information about substances that can serve as a basis for determining whether the products were synthesized or not [49]. TGA and DTG curves of enox, NIP, and MIP to evaluate the thermal stability of the polymer particles are shown in Fig. 6. The thermogram of TG-DTG for enox and all polymers reveals multiple stages of decomposition. An apparent was seen in the thermogram of enox, which shows that the initial decomposition temperature is approximately 40 °C, so this is the first choice to use room temperature (28 °C) for synthesis. MIP TG-DTG data indicate the decomposition at around 41 °C, probably due to enox in the polymer matrix. In NIP, the decomposition process is at a temperature of

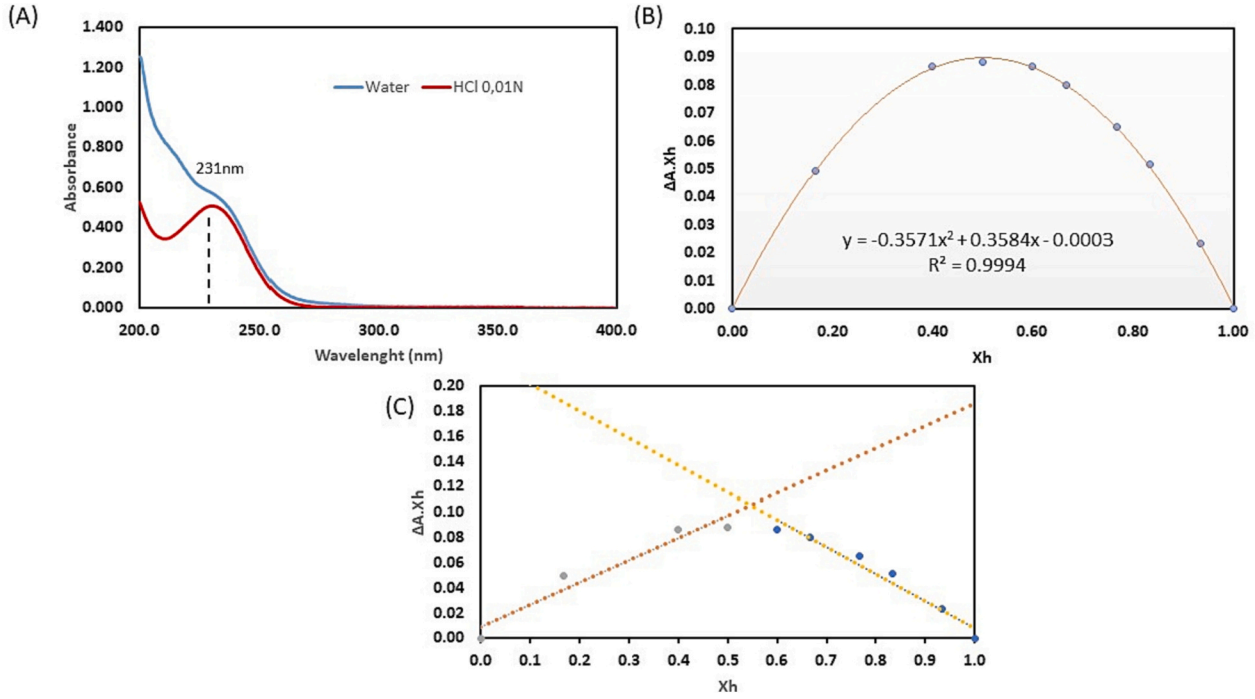

Fig. 5. Experiment study of molar ratio enox between ITA. (A) Solvent for enox, (B) polynomial calculation, and (C) the intersection of two regression lines.

Table 4
Result optimization of time synthesis.

Time (min)	Yield (%)
10	NA
20	NA
30	15.37
60	31.70
90	44.68

Table 5
Result optimization of power magnetic resonance.

Power magnetic resonance (watts)	Yield (%)
300	44.68
400	35.29
500	36.93
600	23.97

Table 6
Result optimization of ratio enox with ITA.

Ratio MIP or NIP		Yield (%)
NIP 1:1	Job's plot and *in silico* MD	91.77
MIP 1:1	Job's plot and *in silico* MD	87.79
NIP 1:4	General ratio	44.68
MIP 1:4	General ratio	40.45
NIP 1:6	DFT and GFN2-xTB	25.67
MIP 1:6	DFT and GFN2-xTB	26.38

approximately 43 °C higher than that in MIP. As shown in Fig. 6, in the temperature range between 24 °C and 300 °C, enox, MIP, and NIP showed weight loss of 59%, 32%, and 30%, respectively. The weight loss of enox is due to the decomposition of surface hydroxyl groups. The lack of weight loss in MIP and NIP compared with that of enox may be caused by the presence of a more stable polymer.

3.2.2.2. SEM. Examining the morphology of polymer particles through SEM analysis is crucial as it offers insights into their size and shape. Fig. 7 presents an SEM image with a magnification of 50,000× of NIP and MIP with varying ratios presenting porous morphology, implying a good performance in adsorption [50]. However, in this method using precipitation polymerization, spherical particles were synthesized using precipitation polymerization is must have [44]. Tamayo et al. proposed that a noncovalent imprinting technique during precipitation polymerization can result in uniformly sized imprinted polymers [51]. The picture also shows the surface of NIP, which appears different from that of MIP. MIP's agglomerate surface is likely due to enox filling the polymer surface. An appearance spherical particle was bigger with more ratio of ITA. The form of MIP and NIP is agglomerated, so the particle size cannot be calculated using SEM. SEM results can be analyzed using image G to see the surface roughness by determining the Ra parameter. Ra is the average overall surface roughness and can be described as the average of the entire distance of the total roughness profile from the centre line within the sampling parameters. The largest Ra value was obtained for a MIP ratio of 1:1, where the rougher the surface, the more excellent the adhesion [52]. Ra Parameter can be seen in Table 7.

3.2.2.3. FTIR spectroscopy. An FTIR technique was used to identify the functional group in the polymer. The FTIR spectrum showed component functional group changes before and after synthesis. Hydrogen interactions between templates and FMs cannot be confirmed by FTIR [53,54]. One sign of polymerization success is the removal of the vibrational absorption peak of the C═C double bond, which becomes a C—C single bond after formation [55]. In 2941–2918 cm^{-1} attributed to the C—H stretching of sp3 carbon. in 1701–1617 cm^{-1} attributed to the C═O stretching of enox, ITA, and MBAA, 1235–1217 cm^{-1} attributed to the S═O stretching of enox and MIP, and 993 cm^{-1} attributed to the C—C stretching. The difference in wavelength 3000–2800 in MIP and NIP occurs because of the enox that has been bound to MIP. The FTIR images are shown in Fig. 8.

3.3. Adsorption capacity

Effect enox solution to determine the maximum adsorption capacity of MIP and NIP sorbent in the adsorption process with a mass of 10 mg

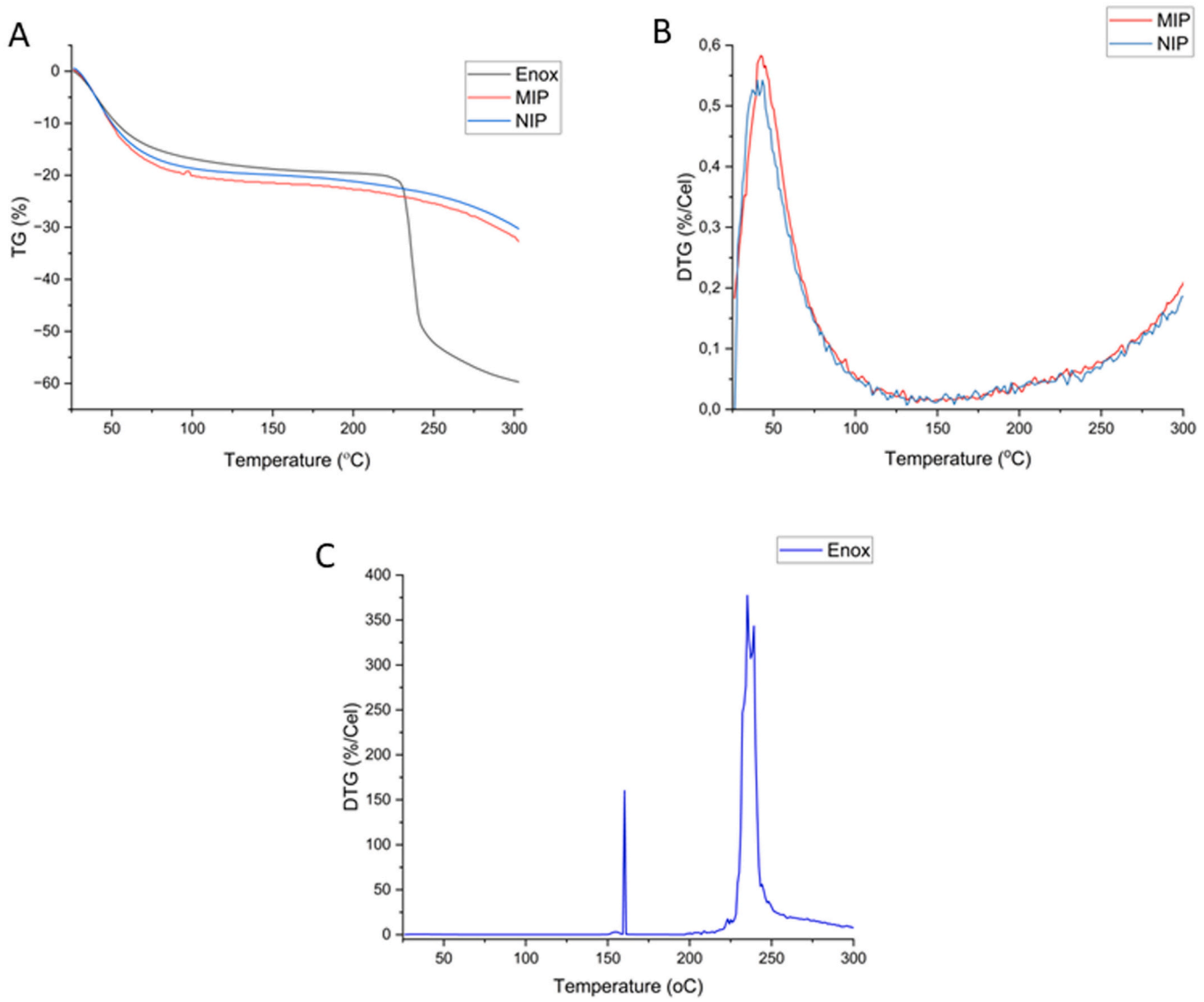

Fig. 6. The results of (A) TGA curves, (B) DTG curve MIP dan NIP and (C) DTG curve Enox.

MIP and NIP sorbents contacted with enox solution at a concentration of 300 ppm for 180 min. This rebinding aims to see MIPs that will be synthesized on a large scale from 1:1, 1:4 or 1:6 for further study and characterization. The concentration of 300 ppm was obtained from a previously validated calibration curve range of between 25 and 500 ppm. Calibration curve can be seen at Fig. 9. The adsorption capacity of MIP 1:1, 1:4, and 1:6 is 43.47 ± 0.40, 24.68 ± 0.46, and 22.31 ± 0.55 mg g^{-1}, respectively. NIP 1:1, 1:4, and 1:6 had adsorption capacities of 36.00 ± 0.30, 35.83 ± 0.50, and 32.36 ± 0.43 mg g^{-1}, respectively. The difference in adsorption capacity between MIP and NIP shows that molecular imprinting determines adsorbent capacity. The imprinting process in MIP creates a molecular-binding area that broadly activates the polymer to molecules, while NIP lacks molecule recognition regions and is nonspecific [56]. Imprinting factors are utilized to evaluate the efficacy of MIP, with higher values indicating superior performance. MIP's performance was deemed satisfactory as it exhibited an *IF* value exceeding 1 [57]. MIP 1:1 has an imprinting factor of 1.21, which is bigger than ratios 1:4 and 1:6, so ratio 1:1 was the best MIP to adsorption enox. The adsorption capacity and imprinting factor result are shown in Table 8.

4. Conclusions

For the first time, this research reports the development of a molecular imprinting polymer (MIP) for enoxaparin that can be synthesized with water solvents using a microwave synthesizer workstation. Enoxaparin is a group of low molecular weight heparin that have never been used in making MIP, whereas other studies only used heparin disaccharide as a template [58]. This research combines the results of *in silico* and experimental calculations to reduce the use of materials and long experiment times in the laboratory. *In silico* results using Gaussian software with *Ab initio* and DFT methods show that the best FM is ITA with the smallest binding and Gibbs free energy. The best ratio of ITA to enox is 1:1 based on molecular dynamics simulation calculations and job's plot experiments. The best optimization of the microwave synthesizer workstation settings for time, magnetic resonance power, and stirring are 90 min, 300 watts, and 400 rpm, respectively, at a fixed set temperature of 28° Celsius. MIP, with a ratio of 1:1, has the best imprinting factor for enox adsorption at a concentration of 300 ppm with a contact time of 180 min and a sorbent mass of 10 mg. This research will continue to characterize and analyze parameters and investigate the use of MIP in preparing samples of blood plasma or drugs containing enoxaparin so that it can be helpful as an adsorbent for

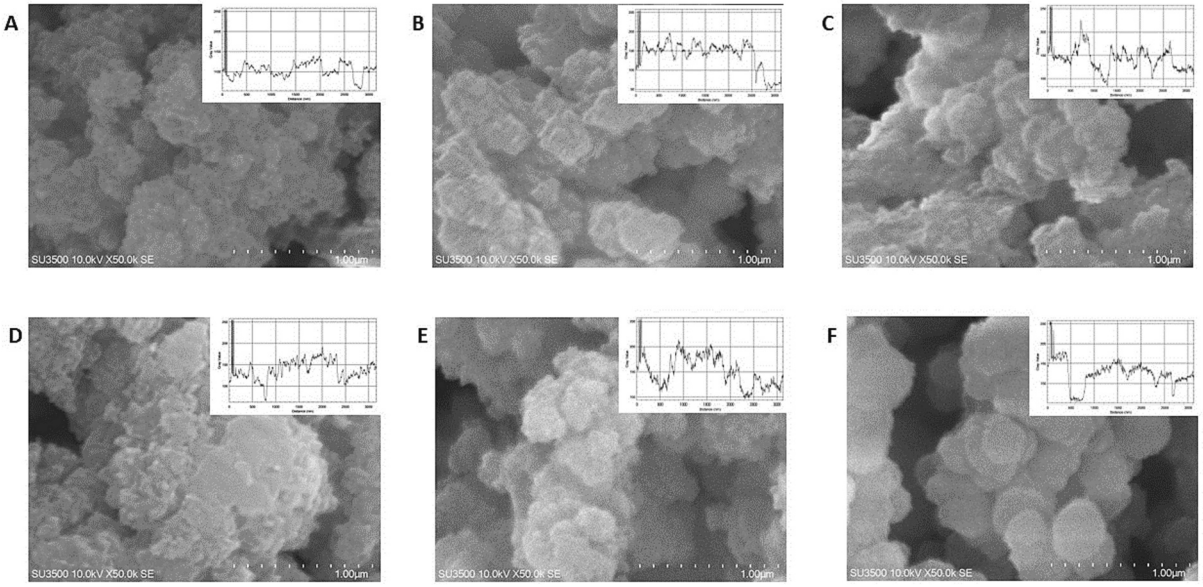

Fig. 7. SEM images of (A) NIP 1:1, (B) NIP 1:4, (C) NIP 1:6, (D) MIP 1:1, (E) MIP 1:4, and (F) MIP 1:6.

Table 7
Ra parameter for surface roughness calculation.

Ratio	1:1	1:4	1:6
NIP	16.2824	15.9953	16.9195
MIP	18.4409	18.4057	15.5482

analyzing enox in drugs or blood plasma.

Author Agreement Statement

We the undersigned declare that this manuscript has not been published previously and is not under consideration for publication elsewhere. We confirm that the manuscript is approved by all authors and tacitly or explicitly by the responsible authorities where the work was conducted, and that, if accepted, this manuscript will not be published elsewhere in the same form, in English or any other language, including electronically without the written consent of the copyright holder.

We understand that the corresponding author is the primary contact for the editorial process. She is willing to handle correspondence at all stages of refereeing and publication, as well as postpublication.

Credit Authorship Contribution Statement

Engrid Juni Astuti: Software, investigation, data curation, and writing–original draft. **Benny Permana:** Formal analysis. **Slamet Ibrahim:** Conceptualization and supervision. **Muhammad Ali Zulfikar**: Methodology and supervision. **Sophi Damayanti**: Conceptualization, supervision, writing–review and editing.

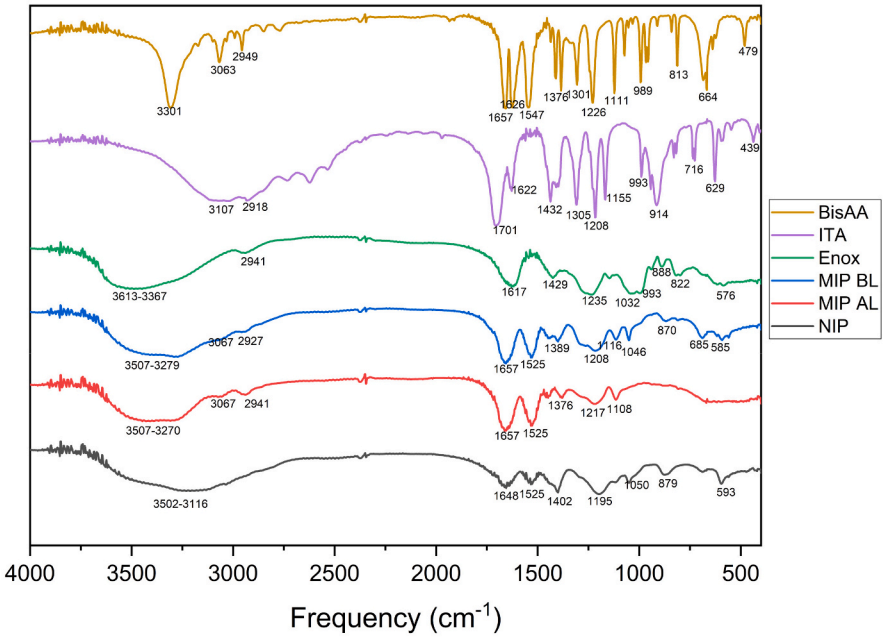

Fig. 8. The FTIR images of enox, MIP, and NIP.

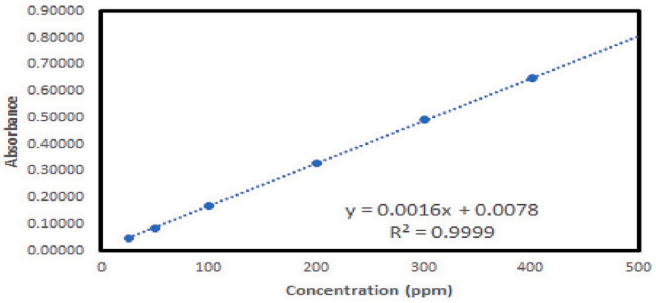

Fig. 9. Calibration curve.

Table 8
Adsorption capacity and imprinting factor results.

Ratio MIP or NIP	Adsorption capacity (mg g^{-1})	*IF*
MIP 1:1	43.47 ± 0.40	1.21
MIP 1:4	24.68 ± 0.46	0.69
MIP 1:6	22.31 ± 0.55	0.69
NIP 1:1	36.00 ± 0.30	
NIP 1:4	35.83 ± 0.50	
NIP 1:6	32.36 ± 0.43	

Declaration of Competing Interest

The authors declare that they have no known competing financial interests or personal relationships that could have appeared to influence the work reported in this paper.

Data availability

Data will be made available on request.

Acknowledgments

The authors are very grateful to the Institut Teknologi Bandung for the financial support of this research study through the ITB Research Program 2022.

References

[1] T. Bayraktutan, Ö.F. Bayraktutan, A novel turn on fluorescence sensor for determination enoxaparin, a low molecular weight heparin, J. Fluoresc. 30 (2020) 1591–1599, https://doi.org/10.1007/s10895-020-02616-w.
[2] C. Shi, C. Wang, H. Wang, C. Yang, F. Cai, F. Zeng, F. Cheng, Y. Liu, T. Zhou, B. Deng, I. Vlodavsky, J.P. Li, Y. Zhang, The potential of low molecular weight heparin to mitigate cytokine storm in severe COVID-19 patients: a retrospective cohort study, Clin. Transl. Sci. 13 (2020) 1087–1095, https://doi.org/10.1111/cts.12880.
[3] A. Vitiello, F. Ferrara, Low molecular weight heparin, anti-inflammatory/immunoregulatory and antiviral effects, a short update, Cardiovasc. Drugs Ther. (2021), https://doi.org/10.1007/s10557-021-07251-6.
[4] W. Miesbach, M. Makris, COVID-19: coagulopathy, risk of thrombosis, and the rationale for anticoagulation, Clin. Appl. Thromb. 26 (2020), https://doi.org/10.1177/1076029620938149.
[5] K. Khownium, J. Romsaiyud, S. Borwornpinyo, P. Wongkrasant, P. Pongkorpsakol, C. Muanprasat, B. Boekfa, T. Vilaivan, S. Ruchirawat, J. Limtrakul, Turn-on fluorescent sensor for the detection of lipopolysaccharides based on a novel bispyrenyl terephtalaldehyde-bis-guanylhydrazone, New J. Chem. 43 (2019) 7051–7056, https://doi.org/10.1039/C9NJ00323A.
[6] O. Zupančič, J.A. Grießinger, J. Rohrer, I. Pereira de Sousa, L. Danninger, A. Partenhauser, N.E. Sündermann, F. Laffleur, A. Bernkop-Schnürch, Development, in vitro and in vivo evaluation of a self-emulsifying drug delivery system (SEDDS) for oral enoxaparin administration, Eur. J. Pharm. Biopharm. 109 (2016) 113–121, https://doi.org/10.1016/j.ejpb.2016.09.013.
[7] A.S. Jeevarathinam, N. Pai, K. Huang, A. Hariri, J. Wang, Y. Bai, L. Wang, T. Hancock, S. Keys, W. Penny, J.V. Jokerst, A cellulose-based photoacoustic sensor to measure heparin concentration and activity in human blood samples, Biosens. Bioelectron. 126 (2019) 831–837, https://doi.org/10.1016/j.bios.2018.11.052.
[8] G.D.O. Silveira, A.M.F. Pego, J. Pereira, E. Silva, M. Yonamine, Green sample preparations for the bioanalysis of drugs of abuse in complex matrices, Bioanalysis. 11 (2019) 295–312, https://doi.org/10.4155/bio-2018-0208.
[9] J.J. Belbruno, Molecularly imprinted polymers, Chem. Rev. 119 (2019) 94–119, https://doi.org/10.1021/acs.chemrev.8b00171.
[10] V. Pichon, N. Delaunay, A. Combès, Sample preparation using molecularly imprinted polymers, Anal. Chem. 92 (2020) 16–33, https://doi.org/10.1021/acs.analchem.9b04816.
[11] H.R. Culver, N.A. Peppas, Protein-imprinted polymers: the shape of things to come? Chem. Mater. 29 (2017) 5753–5761, https://doi.org/10.1021/acs.chemmater.7b01936.
[12] A.-M. Poller, E. Spieker, P.A. Lieberzeit, C. Preininger, Surface imprints: advantageous application of ready2use materials for bacterial quartz-crystal microbalance sensors, ACS Appl. Mater. Interfaces 9 (2017) 1129–1135, https://doi.org/10.1021/acsami.6b13888.
[13] S. Espinoza-Torres, R. López, M.D.P.T. Sotomayor, J.C. Tuesta, G. Picasso, S. Khan, Synthesis, characterization, and evaluation of a novel molecularly imprinted polymer (MIP) for selective quantification of curcumin in real food sample by UV-vis spectrophotometry, Polymers (Basel). 15 (2023), https://doi.org/10.3390/polym15163332.
[14] S. Khan, A. Wong, M. Rychlik, M. del P.T. Sotomayor, A novel synthesis of a magnetic porous imprinted polymer by polyol method coupled with electrochemical biomimetic sensor for the detection of folate in food samples, Chemosensors. 10 (2022), https://doi.org/10.3390/chemosensors10110473.
[15] S. Khan, A. Wong, M.V.B. Zanoni, M.D.P.T. Sotomayor, Electrochemical sensors based on biomimetic magnetic molecularly imprinted polymer for selective quantification of methyl green in environmental samples, Mater. Sci. Eng. C 103 (2019), 109825, https://doi.org/10.1016/j.msec.2019.109825.
[16] M.-O. Simon, C.-J. Li, Green chemistry oriented organic synthesis in water, Chem. Soc. Rev. 41 (2012) 1415–1427, https://doi.org/10.1039/C1CS15222J.
[17] K. Orihara, A. Hikichi, T. Arita, H. Muguruma, Y. Yoshimi, Heparin molecularly imprinted polymer thin flm on gold electrode by plasma-induced graft polymerization for label-free biosensor, J. Pharm. Biomed. Anal. 151 (2018) 324–330, https://doi.org/10.1016/j.jpba.2018.01.012.
[18] X. Zhou, C. Lai, D. Huang, G. Zeng, L. Chen, L. Qin, P. Xu, M. Cheng, C. Huang, C. Zhang, C. Zhou, Preparation of water-compatible molecularly imprinted thiol-functionalized activated titanium dioxide: selective adsorption and efficient photodegradation of 2, 4-dinitrophenol in aqueous solution, J. Hazard. Mater. 346 (2018) 113–123, https://doi.org/10.1016/j.jhazmat.2017.12.032.
[19] L. Zhang, B. Wang, S. Wang, W. Zhang, Recyclable trypsin immobilized magnetic nanoparticles based on hydrophilic polyethylenimine modification and their proteolytic characteristics, Anal. Methods 10 (2018) 459–466, https://doi.org/10.1039/C7AY02418E.
[20] W. Liang, Y. Lu, N. Li, H. Li, F. Zhu, Microwave-Assisted Synthesis of Magnetic Surface Molecular Imprinted Polymer for Adsorption and Solid Phase Extraction of 4-Nitrophenol in Wastewater, 159, 2020, https://doi.org/10.1016/j.microc.2020.105316.
[21] D. Das, A.K. Sarangi, R.K. Mohapatra, P.K. Parhi, A. Mahal, R. Sahu, M. Kudrat-E-Zahan, Aqueous extract of Shikakai; a green solvent for deoximation reaction: mechanistic approach from experimental to theoretical, J. Mol. Liq. 309 (2020), 113133, https://doi.org/10.1016/j.molliq.2020.113133.
[22] A.M. Fahim, E.E.A. Magd, Enhancement of molecular imprinted polymer as organic fillers on bagasse cellulose fibers with biological evaluation and computational calculations, J. Mol. Struct. 1241 (2021), 130660, https://doi.org/10.1016/j.molstruc.2021.130660.
[23] X. Luo, C. Li, Y. Duan, H. Zhang, D. Zhang, C. Zhang, G. Sun, X. Sun, Molecularly imprinted polymer prepared by Pickering emulsion polymerization for removal of acephate residues from contaminated waters, J. Appl. Polym. Sci. 133 (2016) 1–11, https://doi.org/10.1002/app.43126.
[24] K. Karim, T. Cowen, A. Guerreiro, E. Piletska, M.J. Whitcombe, S.A. Piletsky, A protocol for the computational design of high affinity molecularly imprinted polymer synthetic receptors, Glob. J. Biotechnol. Biomater. Sci. 3 (2017) 1–7, https://doi.org/10.17352/gjbbs.000009.
[25] S. Subrahmanyam, S.A. Piletsky, Computational design of molecularly imprinted polymers, in: Comb. Methods Chem. Biol. Sens, 2009, pp. 135–172, https://doi.org/10.1007/978-0-387-73713-3_6.
[26] M. Yadav, A. Shivani, K.K. Ahamad, R. Singh, A. Singh, P. Misra, Tandon, ab-initio and DFT study of HCN: role of temperature for the formation of HCN molecule in the interstellar medium, J. Mol. Struct. 1248 (2022), 131460, https://doi.org/10.1016/j.molstruc.2021.131460.
[27] S. Ansari, Combination of molecularly imprinted polymers and carbon nanomaterials as a versatile biosensing tool in sample analysis: recent applications and challenges, TrAC, Trends Anal. Chem. 93 (2017) 134–151, https://doi.org/10.1016/j.trac.2017.05.015.
[28] S. Ansari, M. Karimi, Novel developments and trends of analytical methods for drug analysis in biological and environmental samples by molecularly imprinted polymers, TrAC, Trends Anal. Chem. 89 (2017) 146–162, https://doi.org/10.1016/j.trac.2017.02.002.
[29] C. Bannwarth, S. Ehlert, S. Grimme, GFN2-xTB - an accurate and broadly parametrized self-consistent tight-binding quantum chemical method with multipole electrostatics and density-dependent dispersion contributions, J. Chem. Theory Comput. 15 (2019) 1652–1671, https://doi.org/10.1021/acs.jctc.8b01176.
[30] C. Paulo, A. Anconi, L. Cristina, A. Souza, Multi-equilibrium approach to study cyclodextrins host – guest systems with GFN2-xTB quantum method: a case study of phosphorothioates included in β -cyclodextrin, Comput. Theor. Chem. 1217 (2022), 113916, https://doi.org/10.1016/j.comptc.2022.113916.

[31] V. Drozd, M. Asadikiya, S. Yang, Y. Zhong, Energy and mechanical properties predictions in Fe-Ni binary system by ab initio calculations, Mater. Today Commun. 33 (2022), 104118, https://doi.org/10.1016/j.mtcomm.2022.104118.
[32] D.H. Utomo, M. Kita, Binding mode of actin–aplyronine A–tubulin heterotrimeric complex revealed by molecular dynamics simulation, Bull. Chem. Soc. Jpn. 96 (2023) 120–126, https://doi.org/10.1246/bcsj.20220299.
[33] J.A. Maier, C. Martinez, K. Kasavajhala, L. Wickstrom, K.E. Hauser, C. Simmerling, ff14SB: improving the accuracy of protein side chain and backbone parameters from ff99SB, J. Chem. Theory Comput. 11 (2015) 3696–3713, https://doi.org/10.1021/acs.jctc.5b00255.
[34] E. Krieger, G. Vriend, New ways to boost molecular dynamics simulations, J. Comput. Chem. 36 (2015) 996–1007, https://doi.org/10.1002/jcc.23899.
[35] M. Paredes-Ramos, F. Bates, I. Rodríguez-González, J.M. López-Vilariño, Computational approximations of molecularly imprinted polymers with sulphur based monomers for biological purposes, Mater. Today Commun. 20 (2019), 100526, https://doi.org/10.1016/j.mtcomm.2019.05.002.
[36] H. Monhemi, M.R. Housaindokht, A. Nakhaei Pour, Effects of natural osmolytes on the protein structure in supercritical CO2: molecular level evidence, J. Phys. Chem. B 119 (2015) 10406–10416, https://doi.org/10.1021/acs.jpcb.5b03970.
[37] D. Li, Assessing the impact of interannual variability of precipitation and potential evaporation on evapotranspiration, Adv. Water Resour. 70 (2014) 1–11, https://doi.org/10.1016/j.advwatres.2014.04.012.
[38] A. Al-Khdhairawi, D. Sanuri, R. Akbar, S.D. Lam, S. Sugumar, N. Ibrahim, S. Chieng, F. Sairi, Machine learning and molecular simulation ascertain antimicrobial peptide against *Klebsiella pneumoniae* from public database, Comput. Biol. Chem. 102 (2023), 107800, https://doi.org/10.1016/j.compbiolchem.2022.107800.
[39] M.M. Rahman, S. Biswas, K.J. Islam, A.S. Paul, S.K. Mahato, M.A. Ali, M.A. Halim, Antiviral phytochemicals as potent inhibitors against NS3 protease of dengue virus, Comput. Biol. Med. 134 (2021), 104492, https://doi.org/10.1016/j.compbiomed.2021.104492.
[40] P. Mattos dos Santos, A.J. Hall, P. Manesiotis, Stoichiometric molecularly imprinted polymers for the recognition of anti-cancer pro-drug tegafur, J. Chromatogr. B Anal. Technol. Biomed. Life Sci. 1021 (2016) 197–203, https://doi.org/10.1016/j.jchromb.2015.12.015.
[41] H.A. Brahmbhatt, A. Surtees, C. Tierney, O.A. Ige, E.V. Piletska, T. Swift, N. W. Turner, Effect of polymerisation by microwave on the physical properties of molecularly imprinted polymers (MIPs) specific for caffeine, Polym. Chem. 11 (2020) 5778–5789, https://doi.org/10.1039/d0py00921k.
[42] L. Chen, X. Wang, W. Lu, X. Wu, J. Li, Molecular imprinting: perspectives and applications, Chem. Soc. Rev. 45 (2016) 2137–2211, https://doi.org/10.1039/C6CS00061D.
[43] S. Fauziah, A.M.M. Gafur, N.H. Soekamto, P. Taba, A. Sapar, Synthesis and characterization of molecularly imprinted polymers of di-(2-Ethylhexyl) phthalate using the precipitation polymerization method, Egypt. J. Chem. 64 (2021) 2385–2392, https://doi.org/10.21608/EJCHEM.2021.44820.2912.
[44] R.M. Roland, S.A. Bhawani, Synthesis and characterization of molecular imprinting polymer microspheres of piperine: extraction of piperine from spiked urine, J. Anal. Methods Chem. 2016 (2016), https://doi.org/10.1155/2016/5671507.
[45] H. Krishnan, A.K.M.S. Islam, Z. Hamzah, P. Nadaraja, M.N. Ahmad, A novel molecular imprint polymer synthesis for solid phase extraction of andrographolide, Indones. J. Chem. 19 (2019) 219–230, https://doi.org/10.22146/ijc.34369.
[46] H.X. He, Q. Gan, C.G. Feng, An ion-imprinted silica gel polymer prepared by surface imprinting technique combined with aqueous solution polymerization for selective adsorption of Ni(II) from aqueous solution, Chinese J. Polym. Sci. (English Ed.) 36 (2018) 462–471, https://doi.org/10.1007/s10118-018-2063-5.
[47] H. Liu, Y. Zhou, Y. Qi, Z. Sun, B. Gong, Preparation of thiamphenicol magnetic surface molecularly imprinted polymers for its selective recognition of thiamphenicol in milk samples, J. Liq. Chromatogr. Relat. Technol. 41 (2018) 868–879, https://doi.org/10.1080/10826076.2018.1531294.
[48] C. Zhang, Y. Wang, Y. Zhou, J. Guo, Y. Liu, Silica-based surface molecular imprinting for recognition and separation of lysozymes, Anal. Methods 6 (2014) 8584–8591, https://doi.org/10.1039/C4AY01657B.
[49] X. Ma, F. Wang, T. Hang, P. Dramou, Degradation study of rutin as template from magnetic composite molecularly imprinted polymer supernatant samples by liquid chromatography–mass spectrometry, J. Chromatogr. A 1673 (2022), https://doi.org/10.1016/j.chroma.2022.463199.
[50] C.F. Silva, L.F. Menezes, A.C. Pereira, C.S. Nascimento, Molecularly imprinted polymer (MIP) for thiamethoxam: a theoretical and experimental study, J. Mol. Struct. 1231 (2021), https://doi.org/10.1016/j.molstruc.2021.129980.
[51] F.G. Tamayo, J.L. Casillas, A. Martin-Esteban, Evaluation of new selective molecularly imprinted polymers prepared by precipitation polymerisation for the extraction of phenylurea herbicides, J. Chromatogr. A 1069 (2005) 173–181, https://doi.org/10.1016/j.chroma.2005.02.029.
[52] C.S. Leão, A.C.R. de Castro, F.M. Copello, C.N. Elias, T. Sekito Junior, E. F. Sant'Anna, Comparison of feldspathic veneer surface treatments on ceramic bracket SBS, ARI and surface roughness after different debonding/polishing methods: an in vitro study, Int. Orthod. 19 (2021) 679–684, https://doi.org/10.1016/j.ortho.2021.08.006.
[53] K. Zhi, L. Wang, Y. Zhang, Y. Jiang, L. Zhang, A. Yasin, Influence of size and shape of silica supports on the sol-gel surface molecularly imprinted polymers for selective adsorption of gossypol, Materials (Basel). 11 (2018) 1–16, https://doi.org/10.3390/ma11050777.
[54] A.N. Hasanah, T.N. Dwi Utari, R. Pratiwi, Synthesis of atenolol-imprinted polymers with methyl methacrylate as functional monomer in propanol using bulk and precipitation polymerization method, J. Anal. Methods Chem. 2019 (2019), https://doi.org/10.1155/2019/9853620.
[55] S. Asman, S. Mohamad, N.M. Sarih, Exploiting F-Cyclodextrin in molecular imprinting for achieving recognition of benzylparaben in aqueous media, Int. J. Mol. Sci. 16 (2015) 3656–3676, https://doi.org/10.3390/ijms16023656.
[56] S. Mishra, D.K. Singh, Th(IV) ion-imprinted polymer for selective solid-phase extraction of Th(IV) and its analytical applications, Desalin. Water Treat. 56 (2015) 1364–1371, https://doi.org/10.1080/19443994.2014.944582.
[57] L. Zhang, H. Zhang, L. Li, P. Zuo, F. Zhao, M. Liu, B.-C. Ye, Y. Li, Pneumocandin B0-imprinted polymer using surface-imprinting technique for efficient purification of crude product, Anal. Sci. 32 (2016) 923–930, https://doi.org/10.2116/analsci.32.923.
[58] R. Zhang, T. Zhang, Y. Lv, P. Qin, H. Li, J. ping Li, T. Tan, Selective binding of heparin oligosaccharides in a magnetic thermoresponsive molecularly imprinted polymer, Talanta. 201 (2019) 441–449, https://doi.org/10.1016/j.talanta.2019.04.050.